

ULTRAVIOLET IMAGING POLARIMETRY OF THE LARGE MAGELLANIC CLOUD. I. OBSERVATIONS

ANDREW A. COLE,^{1,4} KENNETH H. NORDSIECK,^{1,2} STEVEN J. GIBSON,³ & WALTER M. HARRIS²

Draft version November 25, 2018

ABSTRACT

We have used the rocket-borne Wide-Field Imaging Survey Polarimeter (WISP) to image a $1.5^\circ \times 4.8^\circ$ area of the western side of the Large Magellanic Cloud (LMC) at a wavelength of $\lambda = 2150 \text{ \AA}$ and a resolution of $1' \times 1.5'$. These are the first wide-field ultraviolet polarimetric images in astronomy. We find the UV background light of the LMC to be linearly polarized at levels ranging from our sensitivity limit of 4% to as high as $\approx 40\%$. In general, the polarization in a pixel increases as the flux decreases; the weighted mean value of polarization across the WISP field is $12.6\% \pm 2.3\%$. The LMC's diffuse UV background, in uncrowded areas, rises from a minimum of $5.6 \pm 3.1 \times 10^{-8} \text{ erg s}^{-1} \text{ cm}^{-2} \text{ \AA}^{-1} \text{ Sr}^{-1}$ ($23.6 \pm 0.5 \text{ mag arcsec}^{-2}$) to $9.3 \pm 1.1 \times 10^{-8} \text{ erg s}^{-1} \text{ cm}^{-2} \text{ \AA}^{-1} \text{ Sr}^{-1}$ ($23.1 \pm 0.2 \text{ mag arcsec}^{-2}$) in regions near the bright associations. We use our polarization maps to investigate the geometry of the interstellar medium in the LMC, and to search for evidence of a significant contribution of scattered light from OB associations to the diffuse galactic light of the LMC. Through a statistical analysis of our polarization map, we identify 9 regions of intense UV emission which may be giving rise to scattering halos in our image. We find that starlight from the N 11 complex and the LH 15 association are the strongest contributors to the scattered light component of the LMC's diffuse galactic light. This region of the northwestern LMC can be thought of as a kiloparsec-scale reflection nebula in which OB stars illuminate distant dust grains, which scatter the light into our sightline. In contrast, the polarization map does not support the scattering of light from the large B2 complex in the southern WISP field; this effect may be astrophysical, or it may be the result of bias in our analysis.

Subject headings: galaxies: individual (LMC) — polarization — ultraviolet emission — stars: early-type — ISM: structure

1. INTRODUCTION

The presence of extended optical light halos around spiral galaxies raises the question: is this light due to an extended stellar distribution, or is it the result of scattered starlight from more central regions? Jura (1980) pointed out that if the extended clouds of neutral hydrogen around late-type galaxies are associated with dust, the clouds should appear as faint reflection nebulae. In their investigation of the diffuse ultraviolet light of the Galaxy, Murthy & Henry (1995) found a significant contribution due to the scattering of starlight from OB stars by interstellar dust. Photometric studies of spiral galaxies have provided very suggestive evidence for UV scattering halos far from regions of star-formation (Stecher *et al.* 1982, Neff *et al.* 1994). Signatures of dust-scattered starlight are spatial correlations with H I, bluer colors than the general radiation field, and the presence of linear polarization.

The LMC, due to its proximity, vigorous star-forming activity, and low level of obscuration by Galactic dust, is an ideal location in which to investigate the connection between starlight and diffuse light in a spiral galaxy. The LMC is known to possess a higher gas-to-dust ratio than the Galaxy (e.g., Clayton *et al.* 1996); while this would tend to lessen the contribution of scattering to its diffuse galactic light, the relatively high albedo of LMC dust (due

to its depletion in carbon relative to the Milky Way; Pei 1992, Fitzpatrick (1986)) should compensate somewhat.

The Wide-Field Imaging Survey Polarimeter (WISP) instrument is designed to obtain polarimetric images of astronomical objects in the ultraviolet in order to investigate the composition and distribution of dust in astrophysical environments. The ultraviolet is chosen because the emission from late-type stars, which are smoothly distributed and numerous, is suppressed. At optical wavelengths, late-type stars contribute strongly to the general radiation field of a galaxy and may mask the presence of scattered light with their own radiation. In the ultraviolet, OB stars in spatially compact associations dominate the radiation field (e.g., Parker *et al.* 1998 for the LMC); far from these associations, scattered light at these wavelengths is expected to contribute strongly to the diffuse radiation field. In addition to the low stellar background, the UV is an ideal regime in which to make polarimetric investigations because of high polarimetric efficiency (Nordsieck *et al.* 1993).

If scattering is a significant contributor to the diffuse radiation field, then its surface brightness and polarimetric properties can be used to derive information regarding the distribution of dust in the interstellar medium, as well as to place constraints on the optical properties of the dust

¹Department of Astronomy, University of Wisconsin-Madison, 475 North Charter St., 5534 Sterling Hall, Madison, WI, 53706; cole@astro.wisc.edu

²Space Astronomy Laboratory, University of Wisconsin-Madison, 1150 University Avenue, Madison, WI, 53706; khn@sal.wisc.edu

³Department of Physics & Astronomy, University of Calgary, 2500 University Drive NW, Calgary, Alberta, T2N 1N4, Canada.

⁴Current address: Department of Physics & Astronomy, University of Massachusetts, Amherst, MA 01002-4525.

grains.

WISP has been flown three times to date; its targets have been the reflection nebulosity in the Pleiades star cluster (Gibson, Holdaway, & Nordsieck 1995; Gibson 1997), Comet Hale-Bopp (Harris *et al.* 1997), and the LMC.

In this paper, we present polarimetric images of a field along the western side of the LMC. These are the first wide-field ultraviolet polarimetric images ever obtained in astronomy; ground-based imaging polarimetry in the *rest frame* UV of radio galaxies and QSOs at redshifts $z \sim 1$ has been analyzed by, e.g., Cimatti *et al.* (1994), di Serego Alighieri *et al.* (1993), and references therein. Capetti *et al.* (1995) used the Hubble Space Telescope's Faint Object Camera to obtain a UV polarimetric image of the galaxy NGC 1068 with an 11" field of view.

We describe the WISP instrument in §2; in §3 we provide the flight information and observation sequence, and describe the procedures we have adopted for reduction and calibration of the images. §4 gives the results of our surface photometry of the diffuse galactic light of the LMC. In §5 we present our polarization map and our analysis which reveals the scattering halos around some of the prominent concentrations of young stars. In §6 we analyze the morphology of the UV image and polarization map and how it fits in with what is known about the structure and content of the ISM in this region. We discuss in §7 the origin of the diffuse UV radiation field in the LMC and the scattering geometry within the LMC disk; our results are summarized in §8.

2. THE INSTRUMENT

The Wide-field Imaging Survey Polarimeter (WISP) is a suborbital rocket payload based around a 20 cm, F/1.8, off-axis, all-reflective Schmidt telescope. Nordsieck *et al.* (1993) provides a detailed description of the payload optics. The Schmidt corrector mirror removes the spherical aberration of the primary, providing a $1.5^\circ \times 4.8^\circ$ degree field of view with resolution well-suited to the 15 arcsecond pixel scale of the CCD detector. The WISP detector for this flight was a thick, front-illuminated Reticon 400 \times 1200 pixel CCD, phosphor overcoated to provide UV sensitivity. The quantum efficiency of the detector in the vacuum ultraviolet is approximately 15% and the readnoise is 10 e⁻. The CCD was cooled to -65°C by a thermoelectric cooler which dissipates its heat into a copper block which is precooled to -40°C on the ground. WISP has two broadband filters, at $1640 \pm 250 \text{ \AA}$ and $2150 \pm 300 \text{ \AA}$, each comprised of aluminum/MgF₂ thin films on MgF₂ and silica substrates.

The polarimetric analyzer is a large flat mirror mounted between the Schmidt corrector and primary, coated with ZrO₂ (a high-index dielectric), and illuminated at its Brewster angle. The polarimetric modulator is a rotatable 20-cm halfwave plate mounted in the telescope aperture. The waveplate is constructed from four panes of oriented CaF₂ crystal. The crystal is made to be birefringent by applying stress to one side using a programmable actuator. The entire waveplate assembly is then rotated to provide the polarimetric modulation. Four images provide the linear

polarization Stokes parameters: "Q⁺" is obtained with zero waveplate pressure; "Q⁻", "U⁻", and "U⁺" with $\frac{1}{2}$ wave retardation, rotated 45° , 67.5° , and 22.5° relative to the Brewster mirror axis, respectively. Because the modulator is the first element in the WISP optical path, instrumental polarization from subsequent optical elements is eliminated. The position angle zero-point was fixed by optical alignment and mechanical tolerances to better than $\pm 1^\circ$.

Polarimetric calibration was performed in August, 1995 using the 40 cm vacuum collimator at the Space Astronomy Lab, University of Wisconsin. 100% linearly polarized continuum ultraviolet light was created using a D₂ hollow cathode lamp illuminating the focal plane aperture of the collimator, immediately followed by an MgF₂ Brewster-angle polarizer. The polarimetric efficiency of the analyzer is estimated to be better than 98%, based on crossing two analyzers in visible light, and on analysis of the effect of small changes in the Brewster angle in the vacuum ultraviolet. Collimated light from this device illuminated the center and extrema of the WISP field by maneuvering the payload on a remotely controlled tilt table. The efficiency of the WISP analyzer was evaluated by rotating the calibration polarizer with the waveplate off; it is 94% in the 2150 Å filter. The optimal stress for halfwave retardation was evaluated by fixing the calibration polarizer angle and WISP waveplate angle, while varying the waveplate stress. The waveplate efficiency was then evaluated by modeling the polarimetric modulation with waveplate angle at the optimal stress, and found to be 79% in the 2150 Å filter. The net polarimetric efficiency in this filter is therefore $\approx 74\%$; a figure of 70% was used during reductions.

3. DATA

3.1. Flight and Observations

WISP was flown from Woomera, Australia on 17 November, 1995; the flight was a complete success. For the LMC flight the 15" CCD pixels were binned to 4 columns by 6 rows, resulting in an image scale of $1' \times 1.5'$ per pixel. The 2150 Å filter was used to take a polarimetric sequence of 4 80-second exposures, in the order Q⁻, Q⁺, U⁻, U⁺. The science exposures began at an altitude of 230 km, continued through the apogee of 328 km, and ended at 150 km. The planned pointing placed the long axis of the CCD 9° from north-south, with the field centered at $\alpha = 4^\text{h} 58^\text{m} 45^\text{s}$, $\delta = -67^\circ 55'$ (B1950.0). The pointing drifted by less than 5' between the first and last exposures.

3.2. Reduction

We reduced the images within IRAF¹, removing the bias and dark count in the usual way. During the flight, a sequence of 8 bias frames and 3 40-second dark frames were taken for calibration. Additionally, a sequence of 12 dark exposures taken in the laboratory were combined to produce a superdark frame. The lab darks confirmed the linearity of the CCD, and enabled us to better characterize the small-scale variations in pixel response when subtracting the dark frames.

The rocket had begun its descent by the time of the last exposure, and a significant additional sky background was

¹IRAF is distributed by the National Optical Astronomical Observatories, which are operated by the Association of Universities for Research in Astronomy, Inc., under cooperative agreement with the National Science Foundation.

present in the U^+ image. We corrected for this by requiring that the sum of the Q images be equal to the sum of the U images, subtracting the difference in sky background from the U^+ image. The correction amounted to ~ 16 counts, some 7.7% of the total sky background.

We removed cosmic ray contamination in a two-step process. First, we used the IRAF task `cosmicrays` to find and remove pixels which deviated from the median of their neighbors by greater than a factor of ten. These regions were replaced by the mean of their neighbors. The remaining cosmic rays were found during a trial combination of the Stokes images, which rejected pixels that were more than 10σ deviant from the mean across all four images. Deviant pixels were masked off and excluded from further analysis. 10 bright, compact areas of emission, well-distributed across the field of view, were used to align and trim the images. The reduced images were combined to create intensity, Stokes Q , and U images:

$$I = Q^+ + Q^- + U^+ + U^-, \quad (1)$$

$$Q = Q^+ - Q^-, \quad (2)$$

$$U = U^+ - U^-. \quad (3)$$

The intensity image was compared against the catalog of Lucke & Hodge (1970), the atlas of Hodge & Wright (1967), the UV images of Smith *et al.* (1987) (hereinafter SCH), and the catalog of Sanduleak 1970 in order to identify emission sources. We associated 21 bright regions with the OB associations from Lucke & Hodge (1970). Other features include young open clusters, and in some uncrowded regions we detect individual, early-type supergiants (Sanduleak 1970). We placed the image on a world coordinate system using some of these identifications and found the long axis of the image to be aligned 8° east of north. The greyscale intensity image is overplotted on an optical image of the LMC in Figure 1. A schematic figure depicting some of the emission sources is shown in Figure 2.

3.3. Photometric Calibration

SCH presented photometry at 1500 Å and 1900 Å for each association in the Lucke & Hodge (1970) catalog. We used their results to obtain a photometric calibration of our data, using the equation

$$m_{21}^{syn} = m_{19} - (m_{19} - m_{21})_0 - E_{19-21}, \quad (4)$$

where m_{19} refers to the measured 1900 Å magnitude from SCH, $(m_{19} - m_{21})_0$ refers to the intrinsic 1900–2150 Å color of an association, and E_{19-21} denotes the amount of selective extinction between the two wavelengths. m_{21}^{syn} refers to the synthetic 2150 Å magnitude² of each association, calculated from the quantities on the right-hand side of Eq. 4.

For a flat spectrum source with zero reddening, $F_\lambda = \text{constant}$, and Eq. 4 becomes $m_{21}^{syn} = m_{19}$. The two corrective terms arise because the complex spectral energy distribution of the associations and the wavelength-dependent

interstellar extinction distinguish the two filter bandpasses from each other.

The list of calibrating associations is given in Table 1, which includes the magnitude at 1900 Å and 1500–1900 Å color from SCH, the aperture used by SCH, and the E_{B-V} for each association from Lucke (1974).

We dereddened the photometry of SCH, using the value of E_{B-V} from Table 1 and assuming that the maximum contribution of the Galactic foreground was 0.07 mag. Lucke (1974) does not give E_{B-V} for the associations LH 10, 11, 13, or 14 and so we have estimated the reddening to be 0.07. We determined A_{1500}/E_{B-V} and A_{1900}/E_{B-V} by convolving the extinction curves of Cardelli *et al.* (1989) and Fitzpatrick (1986), assuming $R_V = 3.1$, with the source spectrum of a $T_{\text{eff}} = 30,000$ K star (Kurucz 1991) and the filter transmission curves published by SCH. The resulting reddening corrections were:

$$m_{15,0} = m_{15} - 8.82 E_{B-V}^{LMC} - 8.23 E_{B-V}^{MW} \quad (5)$$

$$m_{19,0} = m_{19} - 8.28 E_{B-V}^{LMC} - 8.21 E_{B-V}^{MW}. \quad (6)$$

We then used the calculated $(m_{15} - m_{19})_0$ color, along with stellar atmospheres from Kurucz 1991 and the filter transmission curves of SCH and the WISP 2150 Å filter, to predict the $(m_{19} - m_{21})_0$ color of each association. For OB stars, we adopted a linear relation between the two colors:

$$(m_{19} - m_{21})_0 = 0.57 (m_{15} - m_{19})_0. \quad (7)$$

This relation becomes invalid for sources cooler than $T_{\text{eff}} = 12,000$ K. The intrinsic color of the sources suffers additional reddening due to the well-known extinction bump at 2175 Å. Using the LMC extinction curve of Fitzpatrick (1986) and the Milky Way curve of Cardelli *et al.* (1989), we calculate

$$E_{19-21} = -E_{B-V}; \quad (8)$$

note that because of the 2175 Å bump, $(m_{19} - m_{21})$ becomes *bluer* with increasing extinction³.

Substituting Equations 7 and 8 into Eq. 4, we obtain

$$m_{21}^{syn} = m_{19} - 0.57 (m_{15} - m_{19})_0 + E_{B-V}. \quad (9)$$

The results for each association are given in column 7 of Table 1.

We photometered the associations in the WISP image, attempting to match the apertures to those used by SCH. SCH do not give the precise locations of their apertures, but they provide the area of each region; we matched the areas using rectangular apertures in the IRAF task `polyphot`. The instrumental magnitudes are given in column 6 of Table 1.

We rejected the association LH 20 because it fell along the edge of the field; there was some uncertainty in the position of LH 14. We calibrated our photometry using a least-squares fit to m_{21}^{syn} ; allowing for a nonlinearity as well as zeropoint offset, we found $m_{21}^{syn} = (1.05 \pm 0.10) m_{21}^{inst} - (9.33 \pm 0.24)$, with an rms scatter of 0.26 mag. However,

²We adopt throughout the definition $m_\lambda = -2.5 \log (F_\lambda) - 21.1$.

³The adoption of a mean UV extinction curve is fraught with peril, as well-documented by Fitzpatrick (1998); variation in the extinction curve from sightline to sightline may contribute an additional 20% systematic uncertainty in photometry.

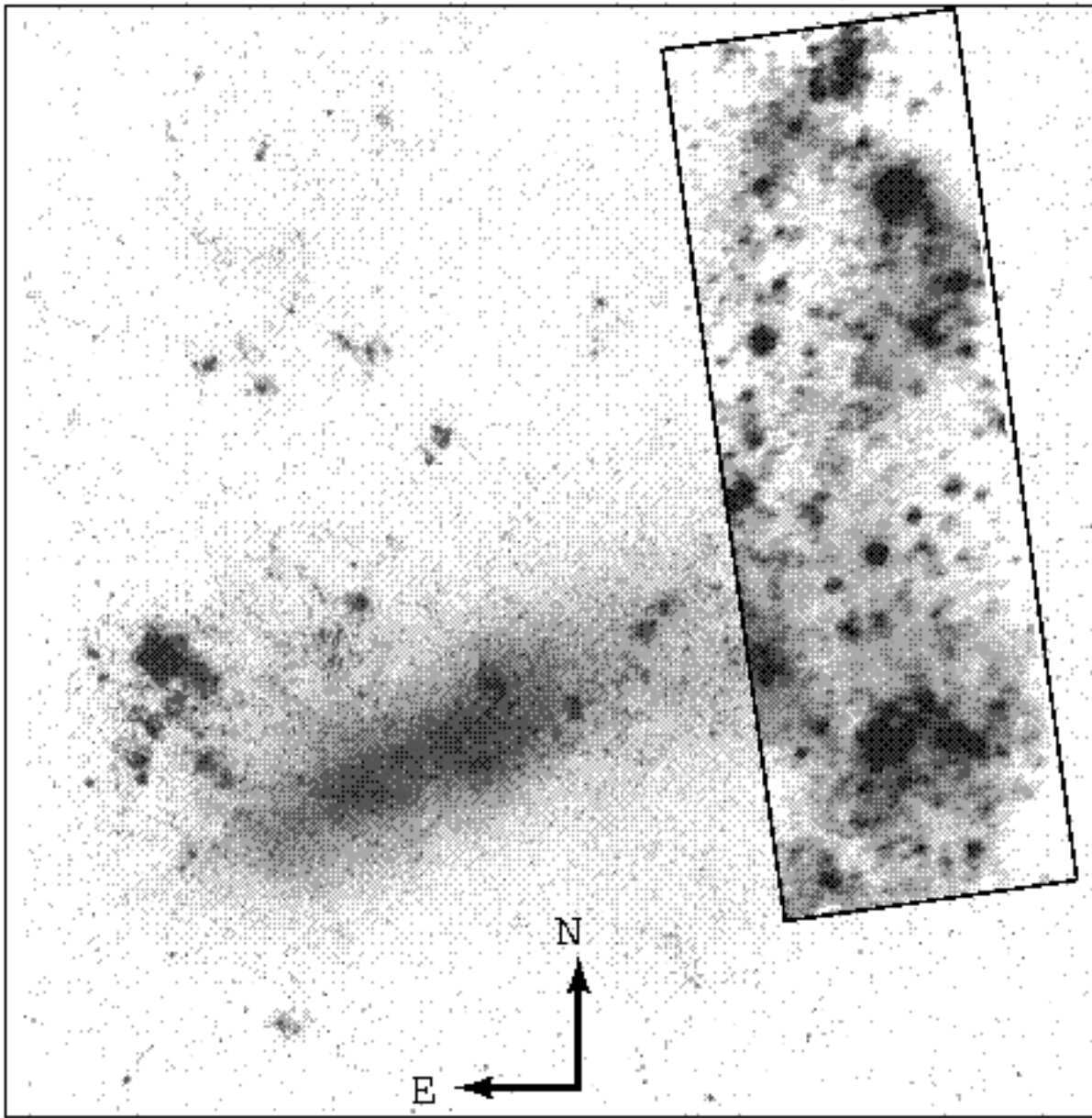


FIG. 1.— The location of the WISP field within the LMC. The underlying optical image ($\lambda \approx 6600 \text{ \AA}$) was taken by Karl Henize; see Sandage (1961). The inset WISP field measures $1^{\circ}5 \times 4^{\circ}8$ and is centered at $\alpha \approx 5$ hours, $\delta \approx -69^\circ$; the center of the LMC is at $\alpha = 5^{\text{h}} 24^{\text{m}}$, $\delta = -69^\circ 48'$.

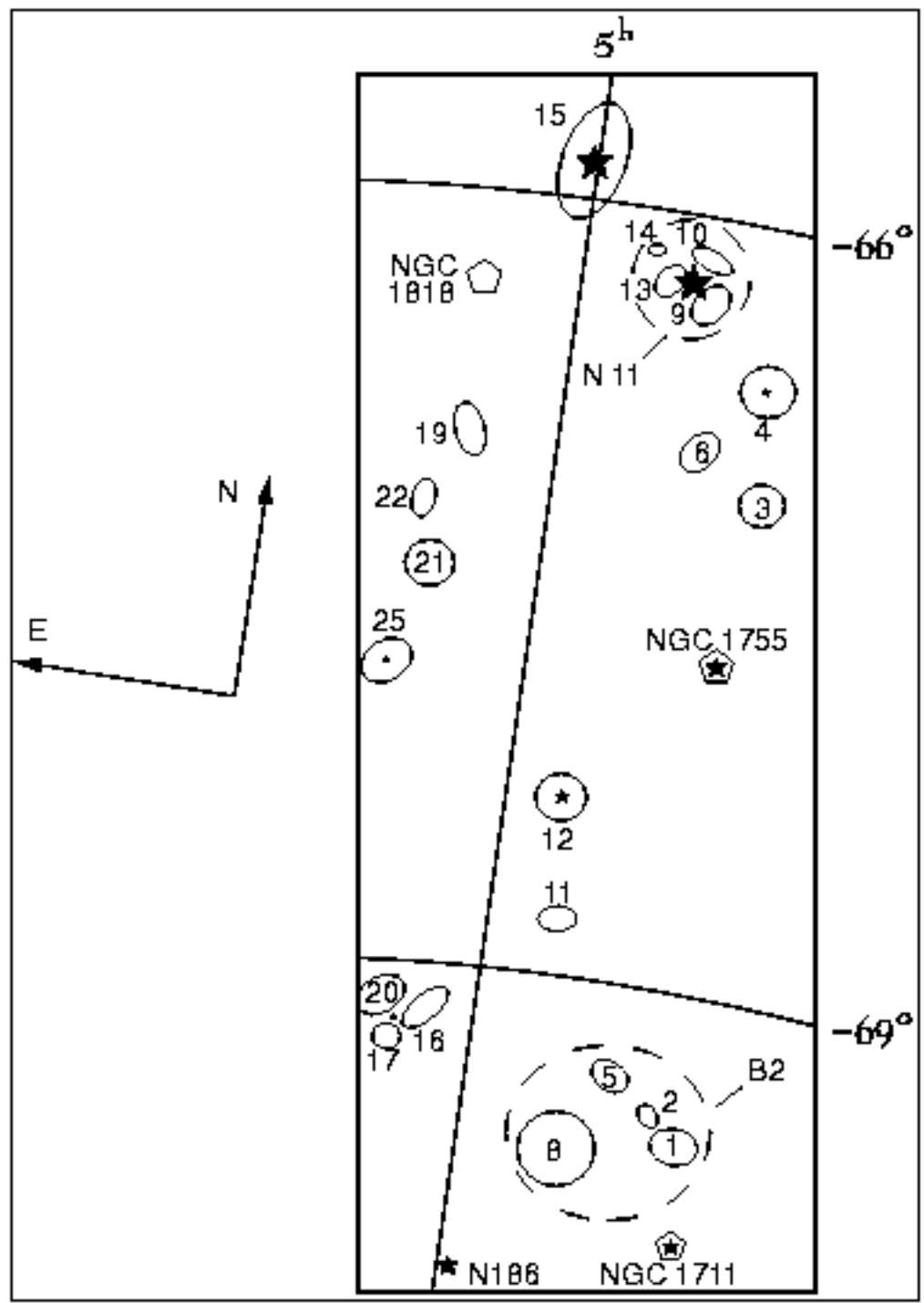


FIG. 2.— Prominent features in the WISP field, after Lucke & Hodge (1970). Numbered ellipses represent the positions of OB associations from Lucke & Hodge; the dashed ellipses N 11 and B2 refer to the enclosed OB associations and emission nebulae. Massive open clusters are denoted by pentagons and labelled with their NGC number. Sources of scattered light from Table 2 are marked with stars; large stars indicate stronger detections.

this fit was only marginally better than one in which we enforced linearity, and which we decided to adopt:

$$m_{21}^{syn} = m_{21}^{inst} - (8.53 \pm 0.28), \quad (10)$$

with an rms scatter of 0.29 mag. For comparison to m_{21}^{syn} , our calibrated photometry for the 20 measured associations is given in column 8 of Table 1. LH 14 was excluded from the fit because of the uncertainty in its identification; it is faint, small, and subject to uncertain sky subtraction due to its close proximity to the extremely bright associations LH 9 and 10.

3.4. Background Subtraction

UV surface brightness measurements are affected by three major sources of background contamination (Murthy & Henry (1995)): zodiacal light, Galactic background light, and the extragalactic background. In order to measure the diffuse galactic light of the LMC, we must remove these background sky levels. Maucherat-Joubert *et al.* (1980) surveyed the entire sky at 2200 Å with 3° resolution, and measured a mean background sky level (Galactic plus extragalactic) of $0.9 \pm 0.2 \times 10^{-8} \text{ erg s}^{-1} \text{ cm}^{-2} \text{ Å}^{-1} \text{ Sr}^{-1}$ for the Galactic latitude of the western LMC ($-35^\circ < b < -38^\circ$). They reported a zodiacal light level at 2200 Å of $0.10 \pm 0.02 \times 10^{-8} \text{ erg s}^{-1} \text{ cm}^{-2} \text{ Å}^{-1} \text{ Sr}^{-1}$ for the LMC's ecliptic latitude. We therefore adopt a total background level of $1.0 \pm 0.2 \times 10^{-8} \text{ erg s}^{-1} \text{ cm}^{-2} \text{ Å}^{-1} \text{ Sr}^{-1}$ ($25.4 \pm 0.3 \text{ mag arcsec}^{-2}$) across the WISP field. This value has been subtracted from each of our surface brightness measures of the LMC's diffuse galactic light.

4. SURFACE PHOTOMETRY

A contour plot of the LMC's surface brightness at 2150 Å is shown in Figure 3, at a resolution of 0.1°. The diffuse UV background, which we attempted to measure in uncrowded areas, rises from a minimum of $5.6 \pm 3.1 \times 10^{-8} \text{ erg s}^{-1} \text{ cm}^{-2} \text{ Å}^{-1} \text{ Sr}^{-1}$ (23.6 ± 0.5 mag arcsec $^{-2}$) to $9.3 \pm 1.1 \times 10^{-8} \text{ erg s}^{-1} \text{ cm}^{-2} \text{ Å}^{-1} \text{ Sr}^{-1}$ (23.0 ± 0.2 mag arcsec $^{-2}$) in regions near the bright associations. The lowest areas occur where the stellar density is low, at the northern edge of the image, along the western edge of the image near -68° , and in the far southwestern corner. Uncrowded regions of high surface brightness include the region between N 11 and LH 19, and the area north of NGC 1755. Regions above the $11 \times 10^{-8} \text{ erg s}^{-1} \text{ cm}^{-2} \text{ Å}^{-1} \text{ Sr}^{-1}$ contour line are highly resolved in the SCH images into sheets of stars; Fig. 3 shows that these high surface brightness regions are clustered around OB associations.

The eastern edge of the image, at roughly -69° , includes the extreme western end of the LMC bar. The bar is prominent in optical images of the galaxy, less so in UV images, e.g., SCH. The stellar density is far higher here than in the northern half of the WISP field; despite the suppression of late-type stars by the UV filter, the densely populated bar contributes to the high UV surface brightness. As will be discussed in §6, this will adversely affect our ability to detect the effects of dust scattering.

Maucherat-Joubert *et al.* (1980) presented a surface brightness map of the LMC at 2200 Å. Agreement between the WISP surface photometry and the Maucherat-Joubert *et al.* (1980) results is surprisingly good, considering the disparity in angular resolution and detector construction,

as well as the uncertainties in photometric calibration. Due to resolution effects, Figure 3 contains more extreme values, both high and low, than the Maucherat-Joubert *et al.* (1980) map; the effect was lessened, although not eliminated, by smoothing the WISP image to 1° resolution. The difference is greatest for the degree-scale arcs seen in the WISP image north of $\approx -67^\circ 30'$: they are blended out by the 3° resolution in the earlier work. The arc containing N 11 is visible in the Maucherat-Joubert *et al.* (1980) map as a small perturbation to the $11 \times 10^{-8} \text{ erg s}^{-1} \text{ cm}^{-2} \text{ Å}^{-1} \text{ Sr}^{-1}$ contour line. In the southern WISP field, the light is more smoothly distributed, and the $16 \times 10^{-8} \text{ erg s}^{-1} \text{ cm}^{-2} \text{ Å}^{-1} \text{ Sr}^{-1}$ contour in Fig. 3 matches the location of the similar isophote in Maucherat-Joubert *et al.* (1980).

5. ULTRAVIOLET POLARIZATION MAP

We mapped the degree of linear polarization, P , and position angle, θ for the WISP field using the I, Q, and U images. Because the direct light of stars contributes highly to the flux but is largely unpolarized, their presence tends to bias the estimates of the polarization of the diffuse galactic light to low values. To remove them from the polarization map, we cleaned the images of pixels that deviated by more than 5σ above the local sky value in all three of the images. The star mask was applied to the individual images and masked pixels were subsequently ignored.

In order to increase the signal-to-noise, we binned the image into 36 arcmin 2 pixels (4 × 6 pixels). For each pixel we calculated the degree of linear polarization:

$$P = \left(\frac{(Q^2 + U^2)}{I^2} \right)^{0.5}, \quad (11)$$

and the position angle, measured clockwise from the positive y -axis (roughly north):

$$\theta = 0.5 \arctan \left(\frac{U}{Q} \right). \quad (12)$$

We assumed Poisson statistics for the calculation of σ_P and σ_θ . Because P is the sum in quadrature of Q and U , the expectation value of P is biased such that for constant Q and U , the most probable measured value of P increases with increasing σ_Q and σ_U . Because our data suffer from poor signal-to-noise levels, we have removed this bias using the formula of Nordsieck (1976). By this formula, a 2.5σ detection is biased so that $P_{obs}/P_{true} \approx 1.1$. We reject as non-detections pixels in which $P < 2.5\sigma_P$. This restriction set our detection limit at 4% polarization.

The final polarization map is shown in Figure 4a. Polarizations as high as 40% are observed in some pixels, although their absolute flux level is small. Most of the values lie between 5% and 20%, with an error-weighted mean $P = 12.6\% \pm 2.3\%$. If we relax the restriction on detections below 2.5σ , the mean $P = 4.4\% \pm 7.8\%$.

The maximum predicted polarization from a commonly used model of the interstellar dust mixture (Mathis, Rumpl, & Nordsieck 1977) is $p_{max} = 0.3\text{--}0.4$ (White 1979). We can estimate the fractional contribution of scattered light to the total UV surface brightness in the WISP field

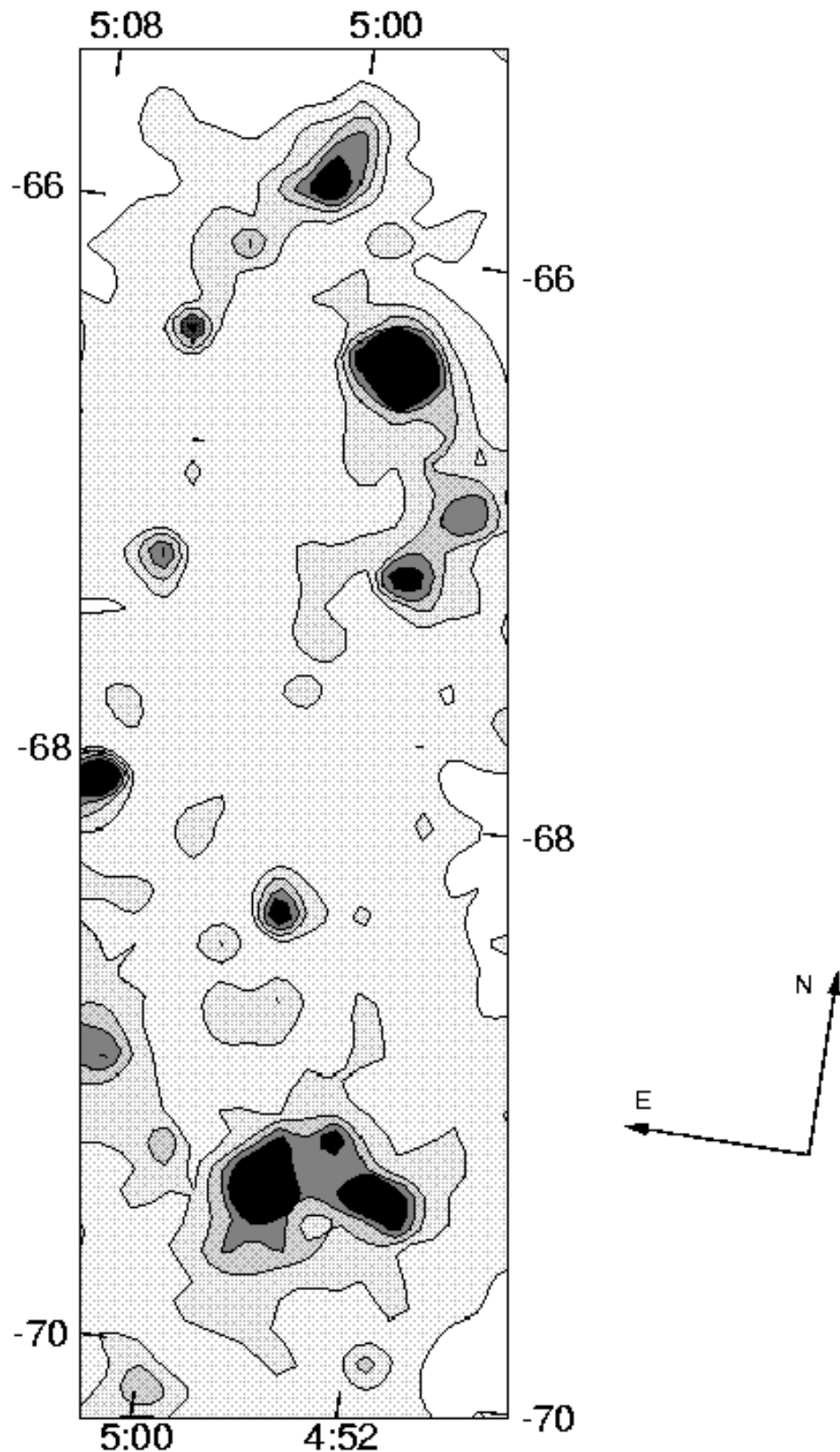


FIG. 3.— Surface brightness plot of the WISP field; the image has been smoothed to 0 $^{\circ}$.1 resolution. North is up and East is to the left. Contour lines are drawn at 6, 11, 16, 21, 26 $\times 10^{-8}$ erg s $^{-1}$ cm $^{-2}$ \AA^{-1} Sr $^{-1}$ (23.5, 22.9, 22.5, 22.2, 21.9 mag arcsec $^{-2}$).

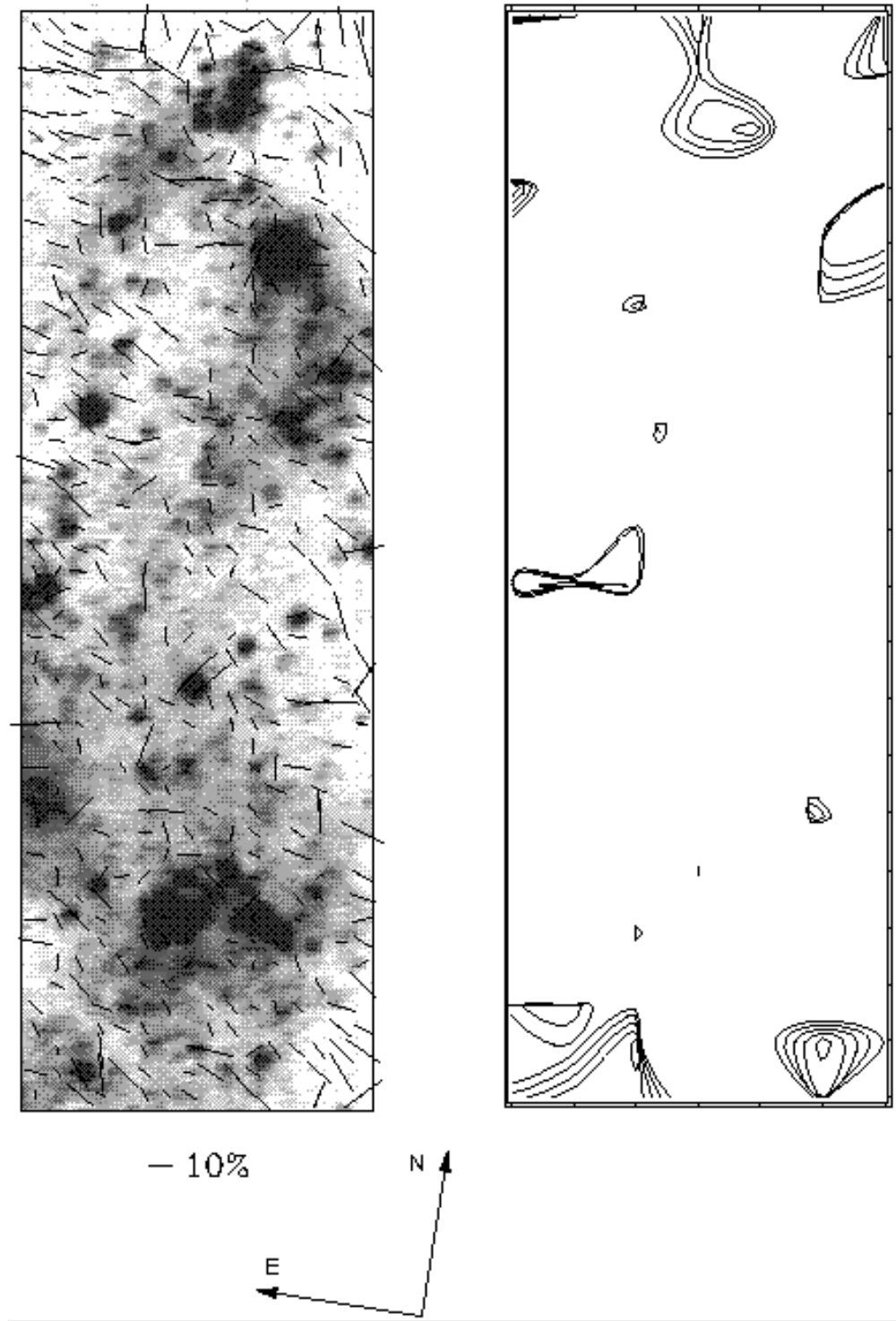


FIG. 4.— a) Ultraviolet polarization map of the WISP field, binned to a resolution of $6'$ per pixel. North is up and East is to the left. Our map becomes incomplete for polarizations below 10%, and our sensitivity limit is 4%. Hints of centro-symmetric scattering patterns can be seen. b) A smoothed contour map of χ^2 , where the χ^2 value of a pixel represents the likelihood that the polarized light in neighboring pixels consists of singly-scattered photons originating in the pixel of interest. Contours are plotted at $\chi^2 = 1,2,3,4,5$.

by comparing our mean P to p_{max} . This comparison suggests that 10–15% of the UV surface brightness is due to polarized scattered light. However, polarization as high as p_{max} occurs only for scattering at a 90° angle, and decreases for smaller and larger scattering angles. Because of the forward-throwing nature of dust grains in the ultraviolet, the mean scattering angle is expected to be much smaller than 90° for our data. The polarization of a scattered photon decreases asymptotically to zero as the scattering angle approaches zero (e.g., Scarrott *et al.* 1990). We therefore predict that much more than 10–15% of the measured UV surface brightness is contributed by scattered photons.

For the case of scattering from a point source, the polarization vectors form a characteristic centro-symmetric pattern around the illuminating source. The typical error in our position angles is $\pm 25^\circ$; this noise distorts the centro-symmetric signature of scattering halos around bright sources, if such features are present. Although our map is noisy, the high mean level of P is indicative of a significant scattered light component to the general UV surface brightness.

To identify the sources most likely responsible for illuminating the interstellar dust, we performed a statistical analysis designed to evaluate the degree of centro-symmetry in the polarization map. We stepped through the polarization map, pixel-by-pixel, and for each pixel, we examined the distribution of polarization vectors in the encompassing 7×7 pixel ($42' \times 42'$) region. For each region, we computed a χ^2 value based on the distribution of $(\theta_{obs} - \theta_{pred})$, compared to the observed position angle errors σ_θ . We thereby created a map of χ^2 values; the χ^2 of a given pixel is a measure of the likelihood that the measured polarizations in neighboring pixels have arisen due to scattered photons originating in the pixel of interest.

The mean value of χ^2 was 8.3×10^3 ; several minima, with χ^2 of order 1–10, were present. To minimize the impact false (noise) minima, we averaged over 6' regions to produce our final χ^2 map (Figure 4b). We have highlighted the regions of low χ^2 by plotting Figure 4b using contours at 1,2,3,4, and 5. The smoothing procedure has failed to eliminate the worst of the false minima, which are typically shallow and spatially compact, or adjoin an edge of the image. Broad but shallow minima which correspond to sources such as LH 4 or NGC 1755 (see Figure 2, Table 2) have been obscured by the smoothing procedure and do not appear in Figure 4b.

We correlated the χ^2 and intensity images in order to identify the birthplaces of scattered photons. During this process, we discovered that the locations of the χ^2 minima and the centroids of the OB associations were, in general, offset from each other. This behavior is expected for light scattered from an extended dust layer, inclined to the line of sight. For the N11 complex, which is the brightest region in the WISP field and lies in a region of low background, the offset between the closest χ^2 minimum and the association centroid was $8.4^{+1.8}_{-5.4}$ arcminutes in the $-x$ direction (roughly west), and 1.8 ± 1.8 arcminutes in the $+y$ direction (roughly north). The other minima showed wide scatter about these values.

The identifications, coordinates, and a brief description of the 9 identified sources of scattered light are given in

Table 2. We also list the value of χ^2 for each object; these values are indicative of the degree to which the polarization patterns near the objects resemble the centro-symmetric halo that would be produced by scattering of starlight from the central objects from a thin disk of material.

6 of the 9 regions are large OB associations or complexes as identified by Lucke & Hodge (1970). Two of the others are large, very young open clusters; the last is an H II region associated with a small starcloud (Henize (1956)); the ionizing star is likely to be the 11th magnitude B1 supergiant Sk $-70^\circ 29$ (Sanduleak 1970). The illuminating sources in Table 2 are marked with star symbols in Figure 2.

Due to our averaging procedure, and because the errors in position angle do not form a normal distribution, our calculated χ^2 values cannot be easily interpreted in absolute terms. We therefore do not place formal confidence limits on our detections of scattering halos around the illuminating sources. However, the χ^2 values listed in Table 2 do accurately reflect the *relative* strengths of the detected scattering halos; the symbol sizes in Fig. 2 have been scaled according to these values.

In sharp contrast to LH 15 and the associations in N 11, the group labelled B2 (notation from Martin *et al.* 1976) corresponds to a broad *maximum* in χ^2 , suggesting that the nearby ISM does not support a scattering halo around the OB stars within. Similarly, the open cluster NGC 1818, which is of a similar age and brightness to the scattered light sources NGC 1755 and NGC 1711, shows no evidence for a scattering halo. These differences are discussed further in §6.

6. ANALYSIS

6.1. Correlations with other wavelengths

The physical interpretation of our UV surface brightness and polarization maps is greatly aided by the consideration of observations at optical, infrared, and radio wavelengths. UV polarization maps probe the structure of the interstellar medium surrounding young, massive stars. Such extremely young stellar populations are often attended by the signatures of recent star formation, such as molecular gas, dark nebulae and emission from heated dust. The dust which both absorbs and scatters the copious UV emission from OB associations is distributed within the neutral hydrogen clouds of the galactic disk. While massive stars are the most luminous, they are dwarfed in number by the less massive stars which form along with them as well as those which have survived from earlier star formation epochs; the combined light of low-mass stars contributes to the UV surface brightness of the LMC, and will tend to dilute the observed polarization.

Dust can be traced directly, via maps of the interstellar extinction and by mapping the radiation from heated dust grains, and indirectly, via maps of the distribution of H I and estimates of the gas-to-dust ratio. In the infrared, it has been found that the $60 \mu\text{m}$ and $100 \mu\text{m}$ data taken by the IRAS satellite correlate well with the H I distribution. As discussed by Sauvage & Vigroux (1991), the bulk of the $60\text{--}100 \mu\text{m}$ emission is due to the dust grains in the general ISM. We note a good correlation between the maps of Schwering (1989) and our UV image; the surface brightness at $60\text{--}100 \mu\text{m}$ and in our Fig. 4 are of the same order

of magnitude, with the IRAS values larger. This confirms that Balmer continuum photons provide the bulk of the energy that heats the interstellar dust.

Maps of the interstellar reddening, e.g., Isserstedt & Kohl (1984), are more sensitive to dust above the plane of the disk than within it, but reveal that high amounts of extinction are present in front of N 11, in the area extending from LH 17 to LH 20, at the end of the stellar bar, and over a large region west of 5^h right ascension and south of $-67^\circ 30'$. There is little apparent correlation between regions of high E_{B-V} and the spiral structure studied by, e.g., deVaucouleurs & Freeman (1972).

The distribution of H I, mapped at low resolution by Luks & Rohlfs (1992) and at high resolution by Kim *et al.* (1998), correlates closely with the IRAS maps; high-column density regions are associated with regions of high E_{B-V} , although the correlation is not perfect. These images are plotted for comparison in Figure 5, along with an optical image. For the direct UV light of OB associations, there is a clear anti-correlation between H I column density and UV brightness; extreme examples are the areas of the supergiant H α shells from Meaburn (1980). The shell LMC 1 surrounds the OB complex LH 15, and light from that association escapes virtually unabsorbed. The same is true for the giant shell around N 11; B2 is surrounded by a network of shells, and LH 12 lies in the wall of the supergiant shell LMC 6. The reason for the anti-correlation is clear; stellar winds and supernovae clear the areas around prominent young associations and clusters. However, when regions far from the large associations are considered, the picture is not as clear.

We examined the maps of Kim *et al.* (1998), looking for correlations between structure in the H I distribution and the UV light. Figure 5 shows that instances can be found where the diffuse UV light closely traces the H I distribution. Three of Meaburn's (1980) supergiant H α shells fall within the WISP field of view and are shown in the lefthand panel of Figure 5. For example, the wall of LMC 1, which extends northeast from N 11, shows a high UV surface brightness; throughout the image, filaments and knots of H I can be identified with UV emission. The lack of H I east-southeast of N 11 is seen as well in the UV; the same is true for the regions north of NGC 1755, and in the extreme southwestern corner of the image. However, counterexamples are present as well; the UV spur extending from LH 15 to NGC 1818 corresponds to a marked lack of H I.

As shown in Figure 5, the optical emission from the general stellar population provides a crucial piece of the puzzle as well. Due to the smoother distribution of late-type stars, the spiral arm structures are much less prominent in the optical image. These stars, while faint in the UV, nevertheless contribute by their sheer numbers to the UV surface brightness. While individual stars are generally beneath our detection threshold, they contribute an unpolarized, unresolved background that will tend to lower our polarization measures. The stellar density is highest in the southeast quadrant of our field, where we see the western end of the LMC's bar. The stellar density falls off rapidly northward of -68° , an impression confirmed by an examination of a starcount map produced from the USNO-A astrometric catalog (Levine & Monet, private communication).

It is apparent that we are looking at a field whose properties show a strong north-south gradient. In the south, the UV light correlates well with general stellar density, identifications with features in the H I and IRAS maps are not obvious, and potential sources of scattered light, such as B2, seem less likely to contribute polarized flux to the UV light. In the north, the field stellar density drops, the UV light correlates somewhat more strongly with the H I surface brightness, and the large, young associations, such as N 11 and LH 15, seem to support extended scattering halos.

6.2. Scattering geometry

Given the general trends with environment explored in the previous section, we now examine the effects of the placement of illuminators and scatterers on the observed polarization map. We wish to uncover the similarities between the sources in Table 2; to discover why the B2 complex and the cluster NGC 1818 seem not to contribute to the polarization map; and to assess the possibility that stars from beyond the WISP field contribute to the scattered light.

The most obvious requirement for the existence of scattering halos around bright associations is the presence of interstellar dust around the associations. The asymmetry of the scattering phase function must also be considered; there is strong evidence for a forward-throwing UV phase function for interstellar dust (e.g., Murthy & Henry (1995), Witt *et al.* 1992). In these cases, back-scattering is suppressed, and associations that lie between the observer and a scattering layer will produce smaller scattered light intensities than associations that lie behind the dust.

The WISP field of view encompasses two of the spiral arms identified by deVaucouleurs & Freeman (1972): arm A extends from LH 15 down east side of our image to LH 17 and is defined by a chain of clusters and associations; arm B extends from N 11 to the B2 complex in the south and is less well-defined in our image. Stecher *et al.* 1982 argued that spiral arms rich in OB associations and H II regions should produce more direct starlight than scattered light in the UV. Additionally, the lack of dust in the LMC's spiral arms (Oestreicher & Schmidt-Kaler (1996)) will tend to suppress scattering.

A common feature of the sources in Table 2 that support scattering halos is their placement within or at the edge of H I giant or supergiant shells. However, given the generally chaotic distribution of H I, this may be a difficult situation to avoid.

One bright UV source that does not support a scattering halo is NGC 1818, prominent in the UV spur containing LH 15. NGC 1818 is 20–40 Myr old (Westerlund 1997), and is brighter than both of the detected clusters NGC 1755 and NGC 1711 ($V_{1818} = 9.70$, $V_{1755} = 9.85$, $V_{1711} = 10.18$; van den Bergh 1981). The region surrounding NGC 1818 is remarkably quiescent in the H I map, and the cluster itself is only moderately reddened, with $E_{B-V} = 0.05$. The IRAS map (Schwering (1989)) also shows little thermal dust emission in the NGC 1818 region. The WISP UV image shows moderate surface brightness around NGC 1818, but in the higher resolution image of SCH, it begins to be resolved into individual stars. We conclude that NGC 1818 is prevented from contributing to the polarization map by a lack of nearby dust.

Figure 5

is available in .gif format
from <http://xxx.lanl.gov/>

FIG. 5.— A multiwavelength view of the western LMC; *far left*: 6600 Å image from a 10 inch refractor (Sandage 1961); *left center*: 2150 Å image from WISP; *right center*: 60 µm image from IRAS (Schwering 1989); *far right*: 21 cm H I image from the ATCA (Kim *et al.* 1998). The locations of supergiant H α shells (Meaburn 1980) are overplotted on the optical image.

The other perplexing association is the large B2 complex in the southern WISP field. Consisting of the Lucke-Hodge associations LH 1, 2, 5, and 8, B2 is nearly the equal of N 11 in the WISP image, and appears to coincide with a high column of H I. The field stellar density around B2 is high, but not as high as around the LH 16-17-20 area; these associations are much smaller than B2 but still show some evidence of a scattering halo.

There is clearly material available to scatter the starlight of B2: its western half is highly reddened, an unambiguous signature of dust. The OB stars of B2 also power several H II regions, most notably N 79 and N 83; these regions are expected to appear as reflection nebulae in the UV. We speculate in passing here that the LH 8 starcloud may not be associated with the rest of B2; it is less highly reddened and contains no large H II regions. Moreover, it is spatially coincident with the LMC 7 supergiant H α shell of Meaburn (1980), corresponding to a hole in the Kim *et al.* (1998) H I maps. There is another large hole in the H I distribution at the western end of the bar (Kim, private communication).

One possibility is that the B2 complex is above the main disk of the LMC, and its scattering halo is therefore suppressed by the forward-scattering phase function of the dust grains. According to the channel maps of Kim *et al.* (1998), most of the H I around B2 lies at a heliocentric velocity of 241–274 km s $^{-1}$. Wayte (1990) has stated that interstellar absorption lines due to LMC gas are present in stars in this region at velocities of \approx 220 km s $^{-1}$, but not at higher velocities, implying that the illuminating stars lie above the main LMC disk.

A further possibility is that the large angular extent of B2 exceeded the limits of the window we used to analyze χ^2 in the polarization map. The 42 arcminute-square window only just contained all of B2, and the point-source approximation we used to test against the distribution of position angles was almost certainly invalid for this case. In addition, most of the window was probably swamped with direct stellar light. We repeated the χ^2 analysis with 54 and 63 arcminute windows, but the results for B2 remained unchanged. The persistent non-detection leads us to suggest that B2 does in fact lie above the main LMC disk, but this is highly uncertain.

The results of our χ^2 test suggest that scattering of light from point sources by a smooth disk cannot be the only source of polarization in the WISP field. In this case, it is possible that light is being scattered from outside the WISP field of view, perhaps from many kiloparsecs away, into our line of sight. Prime candidates for illuminating sources would be the OB associations in Shapley Constellation IV (50' east of LH 19), and the associations in the bar, extending southeast of LH 20. Further afield, the 30 Dor association, postulated by Luks & Rohlfs (1992) to lie as much as 400 pc above the LMC midplane, could be a contributor to scattered light in the WISP field.

To be able to scatter light from associations across the LMC, dust clouds must be raised above the plane of the disk, which is optically thick. Among L $_{\star}$ spirals, galaxies with comparable rates of star formation to the LMC have often had large amounts of dust ejected to distances a kiloparsec or more above the plane (e.g., Howk & Savage 1997). Given the propensity of spiral galaxies for ejecting dust into their halos, and the previously suggested depth

structure of the LMC, it is quite likely that the LMC possesses extraplanar dust; some of this dust may scatter the light of distant OB associations.

7. DISCUSSION

7.1. *To What Extent is the Western LMC a Kiloparsec-Scale Reflection Nebula?*

Several authors have suggested that UV-bright, gas rich galaxies possess extended halos of scattered UV light, in effect creating galaxy-sized reflection nebulae (e.g., Stecher *et al.* 1982, Neff *et al.* 1994). Characteristics of scattered light halos should include somewhat bluer spectral energy distribution than the overall radiation field of the galaxy, a correlation with the H I distribution, and linear polarization. Does the western side of the LMC disk meet any of these criteria?

The WISP field is richer in young stars than the far outer regions of spirals studied by Stecher *et al.* (1982) and Neff *et al.* 1994. Thus any putative scattered light contribution to its UV surface brightness will be diluted by direct, stellar light. In the southern half of the WISP field, the UV surface brightness correlates closely with optical images and with star count maps, suggesting that direct light accounts for most of the ultraviolet radiation. However, northward of $\approx -68^{\circ}$, the stellar density falls off rapidly; Figure 5 shows that the ultraviolet light falls off more slowly. Throughout the image, there are areas of diffuse UV emission that begin to be resolved in the images of SCH, but in the northern WISP field it is easy to see correlations between diffuse UV emission and the presence of H I emission.

The degree to which scattered light contributes to the total UV surface brightness of the LMC can be assessed by examining the mean level of polarization. Our error-weighted mean $P = 12.6\% \pm 2.3\%$; in galactic reflection nebulae, the polarization at optical wavelengths is typically \approx 20–40% (comparable to p_{max} ; e.g., Watkin, Gledhill & Scarrott 1991). We assume that the pixels in which we find $P = 30$ –40% are analogous to reflection nebulae; light that has been scattered nearly in the plane of the sky is the primary contributor to their flux. However, such high values are only found in areas of low flux, and thus high error, in our map.

Because the dust scale height of the LMC disk is non-negligible, and because of the inclination of the disk to the plane of the sky, typical polarization levels should fall below p_{max} . Scarrott *et al.* (1990) showed the variation of P with scattering angle for several dust grain size distributions. Polarization levels of 10–15% are to be expected for scattering angles $\theta \approx 50^{\circ}$ – 60° (and for $\theta \approx 125^{\circ}$ – 135° if backscattering is important). These angles are close to the complement of the LMC's angle of inclination to the sky (28° – 45°), and would be reasonable values for a mean angle of scattering.

As noted in §5, most of our measured polarization values lie between 5% and 20%; this implies that in the average region of the WISP field, at least 20%, and possibly $>90\%$ of the detected light has been scattered. The statistical significance of many of the polarization vectors is low; we seem able to reliably detect polarizations where the contribution of scattered light is $\gtrsim 50\%$.

Jura (1980) presented a method to predict the intensity

of scattered light from a dust cloud at a certain angular distance from an illuminating source. We adapted their method to the case of forward-scattering grains; this model predicts that scattered light surface brightnesses near complexes such as N11 and B2 should lie in the range $0.5 - 1.5 \times 10^{-8} \text{ erg s}^{-1} \text{ cm}^{-2} \text{ \AA}^{-1} \text{ Sr}^{-1}$, within $30'$ of the illuminating sources. This level should be taken as a strict lower limit, since Jura (1980) considered dust clouds in the plane of the sky. Accordingly, the WISP data show surface brightnesses some 4–20 times higher than the Jura (1980) formula predicts. While some of this discrepancy is due to the integrated contribution of scatterers along the line of sight (in front of or behind the plane of the sky), it does suggest that scattered light is not the only contributor to the total surface brightness. The largest difference between the predicted intensity due to pure scattered light and the observed surface brightness occurs for the southern part of the WISP field, where the field stellar density is high.

We conclude from the mean level of polarization and the distributions of UV surface brightness around OB associations that scattered light contributes at least 20% to the total UV surface brightness outside the associations, and possibly more than 50%. The scattered fraction is expected to be higher in the north, where stellar densities are lower and we more confidently detect centro-symmetric polarization patterns around the largest associations. In this respect, the northwestern disk of the LMC can be regarded as a very faint UV reflection nebula. The referee has suggested that similar observations in another bandpass could be a test of this hypothesis. Because of the differing spectral energy distributions of the reflected light of early-type stars and the unresolved sea of late-type stars, an ultraviolet color map could test the idea that the scattered light fraction is higher in the north. Observations at 1500 \AA could be obtained, although the ability to obtain sufficient signal-to-noise is in question.

7.2. What are the Scattering Geometry and Phase Function?

The geometry of the scattering material is of crucial importance for determining the distribution of polarizations. We have seen that the B2 complex shows no evidence for a scattering halo, and suggested a possible geometric explanation. Another issue is the offset of centro-symmetric polarization patterns from the central OB associations, noted in §5. A possible explanation for this offset is the inclination of the LMC disk to the line of sight. The LMC is known to be tilted between 28° and 45° from the plane of the sky, along a roughly north-south axis, with the eastern (30 Dor) side closer to Earth (Westerlund 1997). The effects of varying the inclination of a scattering disk have been investigated by Cole, Wood, & Nordsieck (1999b) in this context, and this explanation does seem plausible.

Another scattering issue that requires modelling is the asymmetry in phase function: do the dust grains scatter isotropically, or are they strongly forward-throwing? If isotropic, the UV surface brightness should fall off more slowly than for the forward-throwing case; the mean polarization level may also change as the preferred paths for

photon escape from the disk are changed. For isotropically scattering grains, the geometric explanation for B2's lack of scattering halo is weakened.

8. SUMMARY

We have obtained the first wide-field ultraviolet polarimetric images in astronomy, using the rocket-borne Wide-Field Imaging Survey Polarimeter (WISP). We find the diffuse UV background light is polarized at levels from 4–40%, the lower limit set by our sensitivity threshold.

We photometrically calibrated our data using the data of Smith *et al.* (1987) for the OB associations of Lucke & Hodge (1970); our photometric accuracy is probably $\pm \approx 20\%$. The UV surface brightness (Fig. 3) is of the same order of magnitude as the IRAS $60\mu\text{m}$ and $100\mu\text{m}$ measures, indicating that Balmer continuum photons are the primary heaters of interstellar dust in the LMC. We find a minimum UV surface brightness of $5.6 \pm 3.1 \times 10^{-8} \text{ erg s}^{-1} \text{ cm}^{-2} \text{ \AA}^{-1} \text{ Sr}^{-1}$ ($23.6 \pm 0.5 \text{ mag arcsec}^{-2}$).

A polarization map (Fig. 4a) was created and analyzed in order to study the diffuse galactic light of the LMC. The mean level of polarization was $P = 4.4\% \pm 7.8\%$; however, we excluded regions where $P < 2.5\sigma$ from the polarization map; the mean of the statistically significant polarization vectors was $P = 12.6\% \pm 2.3\%$. This suggests a mean contribution of scattered light to the total of $>20\%$. We used a modified χ^2 test to identify the sources of scattered light within the WISP field, and found 9 bright regions that might be responsible for scattered light. These are listed in Table 2 and Figure 2.

The fall-off of surface brightness with radial distance from the OB associations was examined and suggests that the scattered light is not the sole contributor to the observed surface brightness. There is a north-south gradient of properties across the field, due to the falloff in stellar density with distance from the bar. The northern half of the image contains the strongest evidence of centro-symmetric polarization patterns and large amounts of scattered light contribute to the UV surface brightness above -68° .

We find that the B2 complex shows no evidence for a contribution to the scattered light around it; it does not support a scattering halo. This may be an effect of the high field stellar density in the neighborhood and unfavorable geometric positioning of stars relative to dust. Alternatively, it may be the result of bias introduced in our analysis of the polarization map.

Many of the questions raised by these data can only be answered at present through modelling efforts. Some of the issues of scattering geometry and phase function will be addressed by Cole, Wood, & Nordsieck (1999b) in an accompanying paper.

WISP is supported by NASA grant NAG5-647. This research has made use of the SIMBAD database of the Centre de Données astronomiques de Strasbourg and NASA's Astrophysics Data System Abstract Service. We would like to thank the anonymous referee whose comments improved the clarity of this paper.

REFERENCES

Capetti, A., Axon, D.J., Macchett, F., Sparks, W.B., & Boksenberg, A. 1995, ApJ, 446, 155.

Cardelli, J.A., Clayton, G.C., & Mathis, J.S. 1989, ApJ, 345, 245.

Cimatti, A., di Serego Alighieri, S., Field, G.M., & Fosbury, R.A.E. 1994, ApJ, 422, 562.

Clayton, G.C., Green, J., Wolff, M.J., Zellner, N.E.B., Code, A.D., Davidsen, A.F., & the WUPPE and HUT Science Teams 1996, ApJ, 360, 313.

Cole, A.A., Wood, K., & Nordsieck, K.H. 1999, *in preparation*.

deVaucouleurs, G., & Freeman, K.C. 1972, *Vistas Astr.*, 14, 163.

di Serego Alighieri, S., Cimatti, A., & Fosbury, R.A.E. 1993, ApJ, 404, 584.

Fitzpatrick, E.L. 1986, AJ, 92, 1068.

Fitzpatrick, E.L. 1998, PASP, in press, astro-ph/9809387.

Gibson, S.J., Holdaway, M.A., & Nordsieck, K.H. 1995, BAAS, 27, 1349.

Gibson, S.J. 1997, BAAS, 191, #32.01.

Harris, W.M., Nordsieck, K.H., Scherb, F., & Mierkiewicz, E.J. 1997, DPS, 29, #32.08.

Henize, K.G. 1956, ApJS, 2, 315.

Hodge, P.W. 1988, PASP, 100, 346.

Hodge, P.W., & Wright, F.W. 1967, *The Large Magellanic Cloud*, (Smithsonian Pr., Washington, D.C.).

Howk, J.C., & Savage, B.D. 1997, AJ, 114, 2463.

Isserstedt, J., & Kohl, W. 1984, A&A, 139, 115.

Jura, M. 1980, ApJ, 241, 965.

Kim, S., Staveley-Smith, L., Dopita, M.A., Freeman, K.C., Sault, R.J., Kesteven, M.J., & McConnell, D. 1998, ApJ, 503, 674.

Kurucz, R.L. 1991, in *Precision Photometry: Astrophysics of the Galaxy*, edited by A.G.D. Phillip, A.R. Upgren, & K.A. Janes (L. Davis Pr., Schenectady), p. 27.

Lucke, P.B. 1974, ApJS, 28, 73.

Lucke, P.B., & Hodge, P.W. 1970, AJ, 75, 171 (LH).

Luks, Th., & Rolhfs, K. 1992, A&A, 263, 41.

Martin, N., Prevot, L., Rebeiro, E., & Rousseau, J. 1976, A&A, 51, 345.

Mateo, M. 1988, ApJ, 331, 261.

Mathis, J.S., Rumpl, W., & Nordsieck, K.H. 1977, ApJ, 217, 425.

Maucherat-Joubert, M., Lequeux, J., & Rocca-Volmerange, B. 1980, A&A, 86, 299.

Meaburn, J. 1980, MNRAS, 192, 365.

Murthy, J., & Henry, R.C. 1995, ApJ, 448, 848.

Neff, S.G., Fanelli, M.N., Roberts, L.J., O'Connell, R.W., Bohlin, R., Roberts, M.S., Smith, A.M., & Stecher, T.P. 1994, ApJ, 430, 545.

Nordsieck, K.H. 1976, ApJ, 209, 653.

Nordsieck, K.H., Marcum, P., Jaehnig, K.P., & Michalski, D.E. 1993, Proc. SPIE, 2010, 28.

Oestreicher, M.O., & Schmidt-Kaler, Th. 1996, A&AS, 117, 303.

Parker, J.W., Hill, J.K., Cornett, R.H., Hollis, J., Zamkoff, E., Bohlin, R.C., O'Connell, R.W., Neff, S.G., Roberts, M.S., Smith, A.M., & Stecher, T.P. 1998, AJ, 116, 180.

Pei, Y.C. 1992, ApJ, 395, 130.

Sandage, A.R. 1961, *The Hubble Atlas of Galaxies*, (Carnegie Inst., Washington, D.C.), p. 38.

Sanduleak, N. 1970, CTIO Contrib., 89.

Sauvage, M., & Vigroux, L. 1991, in IAU Symp. 148, *The Magellanic Clouds*, edited by R. Haynes & D. Milne, (Kluwer Academic Pr., Dordrecht), p. 407.

Scarrott, S.M., Rolph, C.D., Wolstencroft, R.D., Walker, H.J., & Sekiguchi, K. 1990, MNRAS, 245, 484.

Schwingen, P.B.W. 1989, A&AS, 79, 105.

Smith, A.M., Cornett, R.H., & Hill, R.S. 1987, ApJ, 320, 609 (SCH).

Stecher, T.P., Bohlin, R.C., Hill, J.K., & Jura, M. 1982, ApJ, 255, L99.

van den Bergh, S. 1981, A&AS, 46, 79.

Watkin, S., Gledhill, T.M., & Scarrott, S.M. 1991, MNRAS, 252, 229.

Wayte, S.R. 1990, ApJ, 355, 473.

Westerlund, B.E. 1997, *The Magellanic Clouds*, (Cambridge Univ. Pr., Cambridge).

White, R.L. 1979, ApJ, 230, 116.

Witt, A.N., Petersohn, J.K., Bohlin, R.C., O'Connell, R.W., Roberts, M.S., Smith, A.M., & Stecher, T.P. 1992, ApJ, 395, L5.

This figure "AACole.fig5.gif" is available in "gif" format from:

<http://arxiv.org/ps/astro-ph/9909136v1>